Chemical Engineering Journal 503 (2025) 158465

Contents lists available at ScienceDirect

Chemical Engineering Journal

journal homepage: www.elsevier.com/locate/cej

Significantly improving the stability of high-entropy PtFeNiCoMn nanoalloys by nitrogen doping in oxygen electrocatalysis

Mang Niu [a], Qinhe Guan [a], Weiyong Yuan [b], Chun Xian Guo [c], Dapeng Cao [d], Chang Ming Li [c], Lian Ying Zhang [a,*], Xiu Song Zhao [a]

[a] Institute of Materials for Energy and Environment, Institute of Biochemical Engineering, College of Materials Science and Engineering, Qingdao University, Qingdao 266071, PR China
[b] Ningbo Innovation Centre, Zhejiang University, Ningbo 315100, PR China
[c] Institute for Materials Science and Devices, Suzhou University of Science and Technology, Suzhou 215011, PR China
[d] State Key Laboratory of Organic-Inorganic Composites, Beijing University of Chemical Technology, Beijing 100029, PR China

ARTICLE INFO

Keywords:
High-entropy nanoalloys
N doping
Stability
Oxygen reduction reaction
Zn-air battery

ABSTRACT

High entropy alloys (HEAs) possess unique catalytic properties on account of the synergistic effect rooted from the multi-metal components. Many HEA-based materials have been demonstrated to display unprecedented electrocatalytic activities. However, transition metals in HEAs usually suffer from leaching due to the electrochemical oxidation, resulting in a rapid decay in electrocatalytic activity. Here, we report the synthesis of N-doped high-entropy nanoalloys using the rapid Joule heating method. The N-doped quinary PtFeNiCoMn alloy nanoparticles (N/Pt/HEA NPs) exhibit significantly improved durability in the ORR compared to its counterpart without N-doping (Pt/HEA NPs). The advantages on N/Pt/HEA NPs were also observed from the OER and a Zn-air battery full cell. Computational results reveal that fine tuning of the electronic structure of the metals in N/Pt/HEA coupled with the strong N – metal bonds contribute to retarding metal leaching to maintain the observed high catalytic activity.

1. Introduction

High entropy alloys (HEAs) possess unique physical and chemical properties, including catalytic properties [1–3]. Because the electronic states of the elements in HEAs can be modified by controlling elemental composition [4], electrocatalytic properties can be tailored to meet the requirements for a given reaction. In addition, the variation in the coordination environment of the metal components enables HEAs possessing rich active sites and diverse adsorption modes for reactants and intermediate species [5]. In comparison with conventional alloys, the catalytic activity of HEAs shows distinct advantages due to their unique features, such as lattice distortion and sluggish diffusion effects [6].

Noble metals are widely used in electrocatalysis [7,8]. However, the cost of noble metals is of the main concern when it comes to practical applications [9,10]Alloying noble metals with transition metals forming HEA catalysts is an effective strategy for not only lowering the cost but also offering opportunities to modify catalyst properties via tuning electronic structure [11,12], morphology [5], particle size [13], and composition [14,15]. To date, numerous HEA-based structures have been demonstrated to display satisfactory activity levels [16–18]. It should be noted that these electrocatalysts usually suffer from an insufficient durability due to leaching of the transition metals in HEAs, although HEAs present improved chemical and thermal stability compared to normal binary or ternary alloys [19]. To date, rare efforts with in-depth studies are devoted to maintaining the observed high catalytic activity.

Doping light elements (e.g., N, B, and P) in transition metals is an effective strategy for boosting catalytic properties [20–22]. The electronic states of the metal can be modified by the doped light element [23]. It has been shown that the bonding effect between the light element and the metal plays a critical role in improving structural stability [21,22]. In regard to N doping in HEAs, great progress has been made in boosting mechanical properties and corrosion resistance because of the formation of multiple N – metal bonds [24,25]. Nevertheless, the impact of N dopant in noble metal-based HEAs on the properties of oxygen electrocatalysis and assembled Zn-air battery full cell has not been studied. On the other hand, high-temperature thermal treatment and hydrothermal synthesis are of the main methods that are

* Corresponding author.
E-mail address: lyzhang@swu.edu.cn (L.Y. Zhang).

https://doi.org/10.1016/j.cej.2024.158465
Received 12 September 2024; Received in revised form 17 November 2024; Accepted 8 December 2024
Available online 9 December 2024

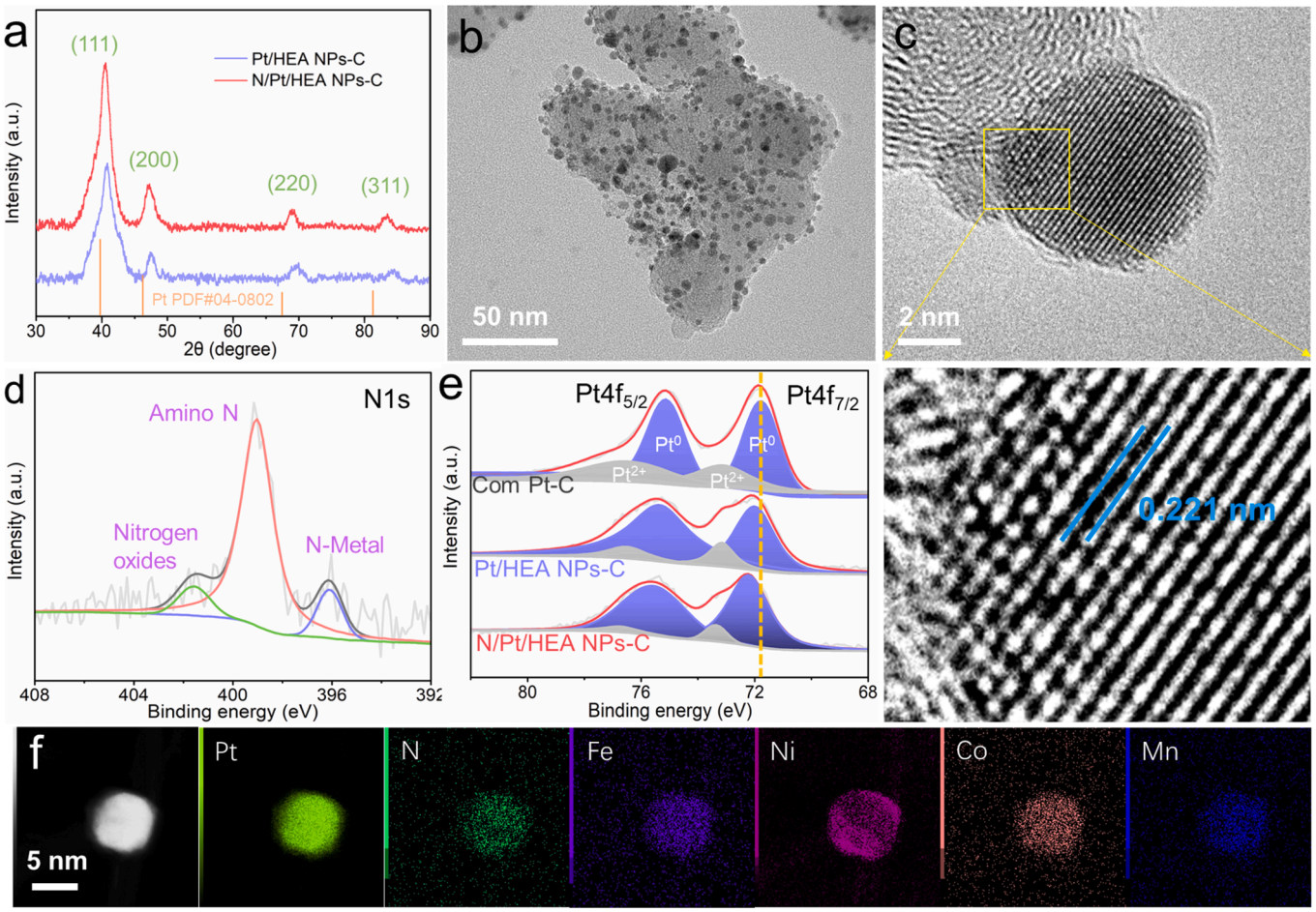

Fig. 1. (a) XRD patterns of Pt/HEA NPs-C and N/Pt/HEA NPs-C. (b) TEM images of N/Pt/HEA NPs-C. (c) TEM images of a single N/Pt/HEA NP and a magnified view of the selected region. (d) XPS spectrum of N 1 s of N/Pt/HEA NPs-C. (e) XPS spectra of Pt 4f of N/Pt/HEA NPs-C, Pt/HEA NPs-C, and Com Pt-C. (f) HAADF-STEM and elemental mapping images of a single N/Pt/HEA NP.

usually used to achieve elemental doping in metals [26]. However, these methods are energy-intensive and/or time-consuming. Rapid Joule heating method has the advantages of low energy consumption, fast heating rate, as well as efficient nucleation and crystallization of nanoparticles [1,27].

The oxygen reduction reaction (ORR) is a key cathodic reaction in metal-air batteries and fuel cells [28–30]; unfortunately, its slow kinetics results in a high overpotential and consequently a low power density [31–33]. Pt is the most widely studied electrocatalyst in ORR [34,35]; nevertheless, it suffers limited catalytic properties. Additionally, high Pt loading is needed to compensate for the sluggish kinetics of ORR [36]. These factors restrict their availability for large-scale commercial implementation [37]. In this study, we used the rapid Joule heating method to synthesize N-doped PtFeNiCoMn HEA nanoparticles (N/Pt/HEA NPs) and investigated their catalytic properties in oxygen electrocatalysis. Results showed that N/Pt/HEA NPs exhibit greatly enhanced catalytic activity and stability toward ORR compared with the PtFeNiCoMn NPs without N doping (Pt/HEA NPs) and Commercial Pt/C catalyst (Com Pt-C). The advantages on the N/Pt/HEA NPs catalyst were also observed from the oxygen evolution reaction (OER) and a Zn-air battery full cell. The remarkable catalytic properties are ascribed to the synergetic effects between the modulated electronic structure of Pt by the N dopant and the formation of N – metal bonds.

2. Experimental section

2.1. Synthesis of carbon supported N-doped quinary PtFeNiCoMn NPs

2.6 mL H_2PtCl_6 solution (7.4 mg mL_{Pt}^{-1}), 10.1 mg $Fe(NO_3)_3{\cdot}9H_2O$, 7.3 mg $Co(NO_3)_2{\cdot}6H_2O$, 4.4 mg $Mn(CH_3COO)_2$, and 58.3 mg of XC-72 carbon were dispersed into 15 mL of ethanol under ultrasonication for over 25 min. Then 14.3 mg $C_{32}H_{16}N_8Ni$ were dissolved into 5 mL dimethylformamide (DMF), followed by adding into above mixture under ultrasonication for another 10 min. The obtained mixed solution was transferred to a vacuum drying oven and dried at 90 °C for 2 h. Finally, the collected sample was heated at 1800 °C using Joule heating equipment in a hydrogen atmosphere. The resulting product was washed and centrifugated over three times with an ethanol/deionized water mixture and the obtained sample was denoted as carbon supported N doped quinary PtFeNiCoMn nanoparticles (N/Pt/HEA NPs-C). N/Pt/HEA NPs-C-1 and N/Pt/HEA NPs-C-2 samples were also synthesized using the same synthetic approaches except that 2.1 mL and 3.0 mL H_2PtCl_6 solutions are fed, respectively.

2.2. Synthesis of carbon supported quinary PtFeNiCoMn NPs

2.6 mL H_2PtCl_6 solution (7.4 mg mL_{Pt}^{-1}), 10.1 mg $Fe(NO_3)_3{\cdot}9H_2O$, 7.3 mg $Co(NO_3)_2{\cdot}6H_2O$, 4.4 mg $Mn(CH_3COO)_2$, 4.6 mg $Ni(NO_3)_2$ and 58.3 mg of XC-72 carbon were dispersed into 20 mL of ethanol under ultrasonication for over 30 min. The obtained mixed solution was transferred to a vacuum drying oven and dried at 90 °C for 2 h. Finally, the collected

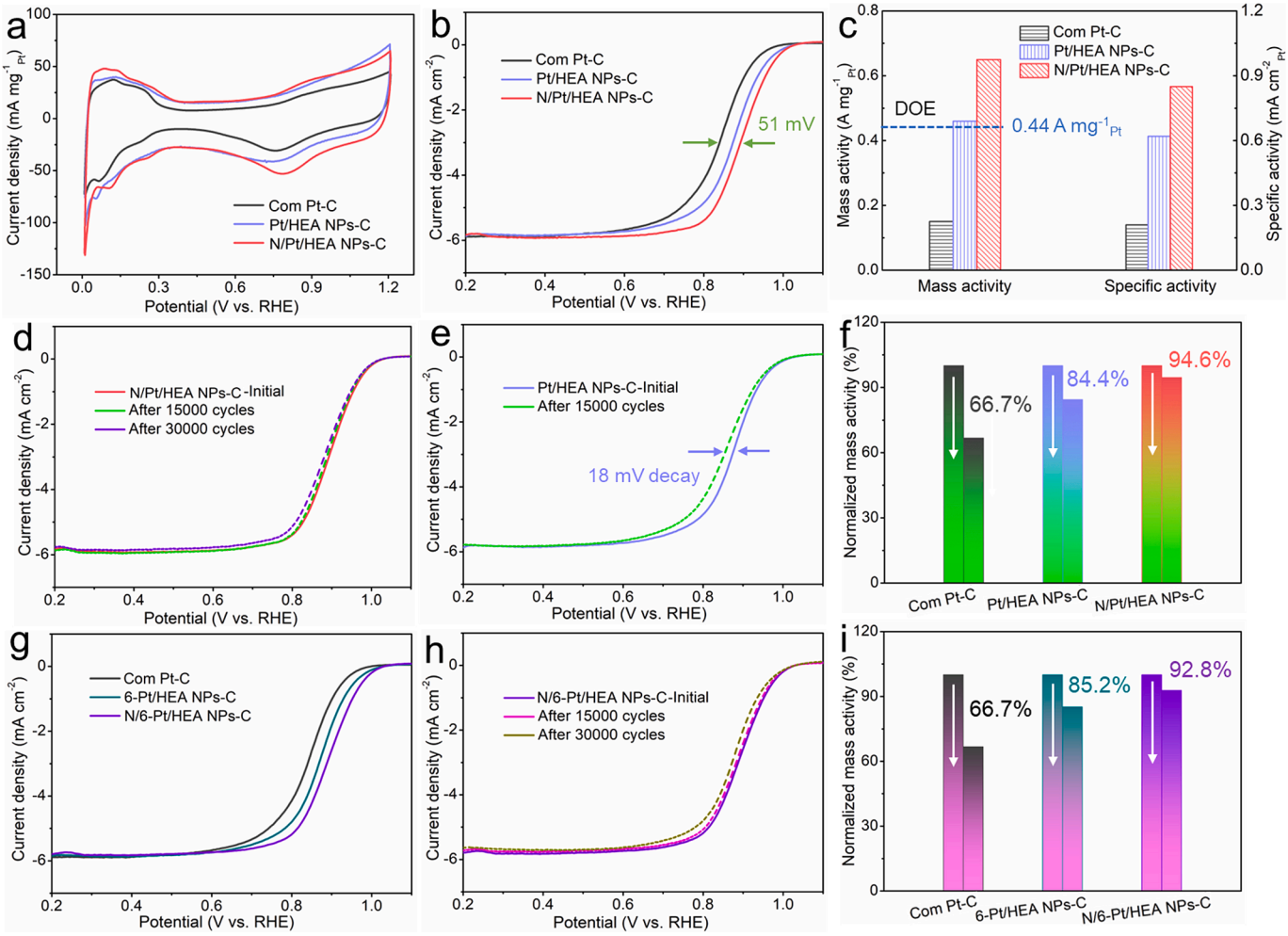

Fig. 2. (a) CV, (b) ORR polarization curves, and (c) activities (0.9 V vs. RHE) of N/Pt/HEA NPs-C, Pt/HEA NPs-C, and Com Pt-C catalysts. ORR polarization curves of (d) N/Pt/HEA NPs-C and (e) Pt/HEA NPs-C before and after stability testing. (f) Normalized mass activity evolutions of various catalysts at half-wave potentials. (g) ORR polarization curves of various catalysts. (h) ORR polarization curves of N/6-Pt/HEA NPs-C before and after stability testing. (i) Normalized mass activity evolutions of different catalysts before and after stability testing at half-wave potentials.

sample was heated at 1800 °C using Joule heating equipment in a hydrogen atmosphere. The resulting product was washed and centrifugated over three times with an ethanol/deionized water mixture and the obtained sample was denoted as carbon supported quinary PtFeNiCoMn nanoparticles (Pt/HEA NPs-C).

2.3. Synthesis of carbon supported N-doped senary PtFeNiCoMnCu NPs

2.6 mL H_2PtCl_6 solution (7.4 mg mL^{-1}_{Pt}), 10.1 mg $Fe(NO_3)_3{\cdot}9H_2O$, 7.3 mg $Co(NO_3)_2{\cdot}6H_2O$, 4.4 mg $Mn(CH_3COO)_2$, 6.0 mg $Cu(NO_3)_2{\cdot}3H_2O$, and 58.3 mg of XC-72 carbon were dispersed into 15 mL of ethanol under ultrasonication for over 25 min. Then 14.3 mg $C_{32}H_{16}N_8Ni$ were dissolved into 5 mL dimethylformamide (DMF), followed by adding into above mixture under ultrasonication for another 10 min. The obtained mixed solution was transferred to a vacuum drying oven and dried at 90 °C for 2 h. Finally, the collected sample was heated at 1800 °C using Joule heating equipment in a hydrogen atmosphere. The resulting product was washed and centrifugated over three times with an ethanol/deionized water mixture and the obtained sample was denoted as carbon supported N doped quinary PtFeNiCoMn nanoparticles (N/6-Pt/HEA NPs-C).

2.4. Synthesis of carbon supported senary PtFeNiCoMnCu NPs

2.6 mL H_2PtCl_6 solution (7.4 mg mL^{-1}_{Pt}), 10.1 mg $Fe(NO_3)_3{\cdot}9H_2O$, 7.3 mg $Co(NO_3)_2{\cdot}6H_2O$, 4.4 mg $Mn(CH_3COO)_2$, 6.0 mg $Cu(NO_3)_2{\cdot}3H_2O$, 4.6 mg $Ni(NO_3)_2$ and 58.3 mg of XC-72 carbon were dispersed into 20 mL of ethanol under ultrasonication for over 30 min. The obtained mixed solution was transferred to a vacuum drying oven and dried at 90 °C for 2 h. Finally, the collected sample was heated at 1800 °C using Joule heating equipment in a hydrogen atmosphere. The resulting product was washed and centrifugated over three times with an ethanol/deionized water mixture and the obtained sample was denoted as carbon supported quinary PtFeNiCoMn nanoparticles (6-Pt/HEA NPs-C).

3. Results and discussion

3.1. Nanostructure and morphology characterization

X-ray diffraction (XRD) patterns were recorded to characterize the crystal structure of N/Pt/HEA NPs-C and Pt/HEA NPs-C and the results are shown in Fig. 1a. For the monometallic Pt crystal (PDF#04–0802), the diffraction peaks at 39.76°, 46.24°, 67.45°, and 81.29° correspond to the Pt(111), Pt(200), Pt(220), and Pt(311) facets, respectively. These features reveal its typical face center cubic (FCC) crystalline structure [38,39]. By contrast, all diffraction peaks of Pt/HEA NPs-C shifted

toward higher angels two theta, indicating a lattice contraction due to the smaller atomic radii of Fe (1.26 Å), Ni (1.25 Å), Co (1.25 Å) and Mn (1.37 Å) than that of Pt (1.39 Å). Interestingly, all diffraction peaks of N/Pt/HEA NPs-C moved toward lower angles two theta compared to that of Pt/HEA NPs-C, implying that the lattice parameters of N/Pt/HEA NPs are expanded due to N doping. This finding is consistent with that observed from the N-doped Pt and Pd nanocrystals in literatures [22,40]. No diffraction peaks of other metals were detected, suggesting that the five metals in the two samples form an alloy phase. The atomic ratio of Pt/Fe/Ni/Co/Mn in N/Pt/HEA NPs determined from the inductively coupled plasma-optical emission spectrometry (ICP-OES) result is 46.42/11.94/14.75/17.22/9.67. These results indicate the formation of Pt-based HEA successfully.

Fig. 1b and S1a show that the N-doped HEA NPs are uniformly distributed on the XC-72 carbon support. The crystal sizes range from 3 to 8 nm (Figure S1b). The well-defined lattice fringe seen from Fig. 1c demonstrates its high crystallinity. The discontinuous atomic arrangement in the crystal lattice indicates the existence of atomic vacancies (Figure S1c), which should be related to the feature of lattice distortion effect in HEA-based materials [41]. The distance of adjacent lattice fringes is 0.221 nm, corresponding to the (1 1 1) facets [42]. In comparison with the monometallic Pt crystal (0.226 nm), the reduced lattice distance of N/Pt/HEA NPs implies the lattice contraction and the existence of a certain compressive strain, which concur with above XRD results. While for Pt/HEA NPs-C, the atomic ratio of Pt/Fe/Ni/Co/Mn determined by ICP-OES is 48.30/15.71/15.90/13.44/6.65. Pt/HEA NPs have a great dispersion on carbon support and similar crystal size distribution to N/Pt/HEA NPs (Figure S2a). The Pt/HEA NP in Figure S2b has a high crystallinity; however, the adjacent lattice fringe decreases to 0.218 nm compared to that of N/Pt/HEA NPs. It is known that a light element tends to be an interstitial dopant in lattice structure of noble metals rather than substitutional dopants by occupying the largest available interstitial sites [23]. The relatively bigger lattice distance of N/Pt/HEA NPs should be related to the interstitial doping of N [43], consistent with the XRD result in Fig. 1a. These results demonstrate that the dopant N has an inconsequential effect on the crystal size, distribution, and even crystallinity of Pt-based HEA NPs.

The X-ray photoelectron spectroscopy (XPS) technique was employed to gain insights into the surface composition and chemical states of different elements in N/Pt/HEA NPs-C. It is seen from Fig. 1d,e and S3 that N, Pt, Fe, Ni, Co, and Mn elements can be detected from N/Pt/HEA NPs-C, with the atomic ratio of 13.29:39.86:7.29:13.23:18.85:7.48. The atomic ratio of Pt/Fe/Ni/Co/Mn is close to its ICP-OES result. For the N 1 s XPS spectrum, three kinds of N species could be distinguished. The N 1 s peak at 399.1 and 401.6 eV respectively corresponds to amine N and N − O bonding, and the peak at 396.5 eV is assigned to N − Metal bonding [44]. This finding gives further evidence for the doping of N into Pt-based HEA. Pt in both N/Pt/HEA NPs-C and Pt/HEA NPs-C is mainly in its metallic state. However, the Pt $4f_{5/2}$ and Pt $4f_{7/2}$ peaks of the former sample shift to more negative positions compared to those of the latter one. The shift should be related to the heteroatom N doping and the result demonstrates that the dopant N can significantly modulate Pt electronic state. In comparison with Com Pt-C, the two peaks of Pt/HEA NPs-C exhibit obviously negative shift, indicating that Pt electronic state can also be altered by the incorporation of transition metals. HAADF-STEM and elemental mapping images in Fig. 1f show that N, Pt, Fe, Ni, Co, and Mn elements have a great dispersion on the nanoalloy, indicating a homogeneous solid solution formed in the sample. Combining with the XRD analysis in Fig. 1a, it can be speculated that the N doped quinary PtFeNiCoMn HEA was prepared successfully. Ni and Co elements in N/Pt/HEA NPs-C are mainly in the form of metallic states (Figure S3a,b), while the Fe and Mn elements in N/Pt/HEA NPs-C mainly exist in the form of oxidation states (Figure S3c,d). Similarly, the XPS spectra in Figure S4 reveal that Ni and Co elements in Pt/HEA NPs-C are mainly in metallic states and Fe and Mn elements mainly in oxidation states. Raman spectra were also performed to investigate the binding information of Pt-based HEA NPs and the Com Pt-C (Figure S5). The minor peaks at ~ 807.8 cm^{-1} correspond to Pt-O or Pt-OH species. While for N/Pt/HEA NPs-C and Pt/HEA NPs-C, the peaks at ~ 557.5 cm^{-1} should be related to the oxide species of introduced transition metals [45–47].

3.2. Electrocatalytic properties for ORR

CV curves were recorded to estimate the electrochemically active surface area (ECSA) of the N/Pt/HEA NPs-C and Pt/HEA NPs-C catalysts (Fig. 2a). ECSA is a critical parameter indicating the number of active sites in electrocatalysts [48–50]. The ECSA values of Pt-based catalysts can be obtained by integrating the charges in hydrogen adsorption/desorption regions after the correction of double-layer adsorption [51], and the parameter of 210 mC cm^{-2} was assumed for monolayer hydrogen adsorption [52]. N/Pt/HEA NPs-C presents an outstanding ECSA up to 76.9 m^2 g_{Pt}^{-1}, which is obviously higher than that of the Com Pt-C (68.7 m^2 g_{Pt}^{-1}) and Pt/HEA NPs-C (74.3 m^2 g_{Pt}^{-1}). Therefore, the developed N/Pt/HEA NPs-C in this work is expected with great catalytic activity. It is noted that the redox peaks of Pt/HEA NPs-C exhibit significant changes in comparison with that of Com Pt-C, and the reduction potential of oxide layer of N/Pt/HEA NPs-C shifts to a more positive position compared to that of Pt/HEA NPs-C. These findings reveal that the dopant N and introduced transition metals play major roles in modulating the electronic structure of Pt and consequently shifting the redox peaks.

There are two distinguishable potential regions in ORR curves (Fig. 2b), the diffusion-limiting current region below 0.7 V and the mixed kinetic-diffusion control region between 0.7 and 1.1 V. It is observed that N/Pt/HEA NPs-C (0.894 V) shows 18 and 51 mV positive shift in half-wave potentials than Pt/HEA NPs-C (0.876 V) and Com Pt-C (0.843 V), respectively, demonstrating its faster reaction kinetics in the ORR. Fundamentally, the ORR activity includes mass and specific activities, which can be evaluated by normalizing kinetic current with respect to ECSA and the amount of Pt loading, respectively [38]. The kinetic current can be calculated via the mass-transport correction using the Levich–Koutecky equation: $1/i = 1/i_k + 1/i_d$, of which i_k represents kinetic current and i_d stands for the diffusion-limiting current [48]. The mass activity of N/Pt/HEA NPs-C at 0.9 V is 0.65 A mg_{Pt}^{-1}, which is 1.4 and 4.3 times greater than those of Pt/HEA NPs-C (0.46 A mg_{Pt}^{-1}) and Com Pt-C (0.15 A mg_{Pt}^{-1}), respectively (Fig. 2c). It is worthy of a note that this value is 1.5 times higher than the target in 2025 set by U.S. Department of Energy (DOE) (0.44 A mg_{Pt}^{-1}). For specific activity, the former (0.85 A cm_{Pt}^{-2}) shows 1.4 and 4.0-fold higher values when compared to the control samples of Pt/HEA NPs-C (0.62 A cm_{Pt}^{-2}) and Com Pt-C (0.21 A cm_{Pt}^{-2}). To understand the impact of Pt loading in N/Pt/HEA NPs-C on ORR activity, the carbon supported N-doped Pt HEA NPs with optimized metal compositions including N/Pt/HEA NPs-C-1 (atomic ratio of Pt/Fe/Ni/Co/Mn: 38.22/13.45/16.29/18.34/13.7) and N/Pt/HEA NPs-C-2 (atomic ratio of Pt/Fe/Ni/Co/Mn: 53.06/10.31/13.89/11.82/10.92) were synthesized. The mass activities of N/Pt/HEA NPs-C-1 and N/Pt/HEA NPs-C-2 are 0.54 and 0.61 A mg_{Pt}^{-1}, respectively (Figure S6). Both of which are lower than that of N/Pt/HEA NPs-C. The electrochemical impedance spectra (EIS) in Figure S7 exhibited that both N/Pt/HEA NPs-C (~ 30.0 Ω) and Pt/HEA NPs-C (~ 31.9 Ω) have a lower charge transfer impedance the Com Pt-C (~ 34.5 Ω).

The electrochemical stability of N/Pt/HEA NPs was also estimated via the accelerated durability testing (ADT) by continuous 15,000 cycles. Interestingly, the ORR profiles of N/Pt/HEA NPs-C before and after the ADT almost overlap (Fig. 2d), illustrating a negligible half-wave potential decay and consequently an excellent electrochemical durability. By contrast, for the Pt/HEA NPs-C (Fig. 2e) and Com Pt-C catalysts (Figure S8), 18 and 36 mV losses in half-wave potentials were observed after ADTs. Only 10 mV decay in half-wave potential was observed for N/Pt/HEA NPs-C even when the cycle number in the ADT increased to 30000. Besides half-wave potential decay, the ORR activity attenuation

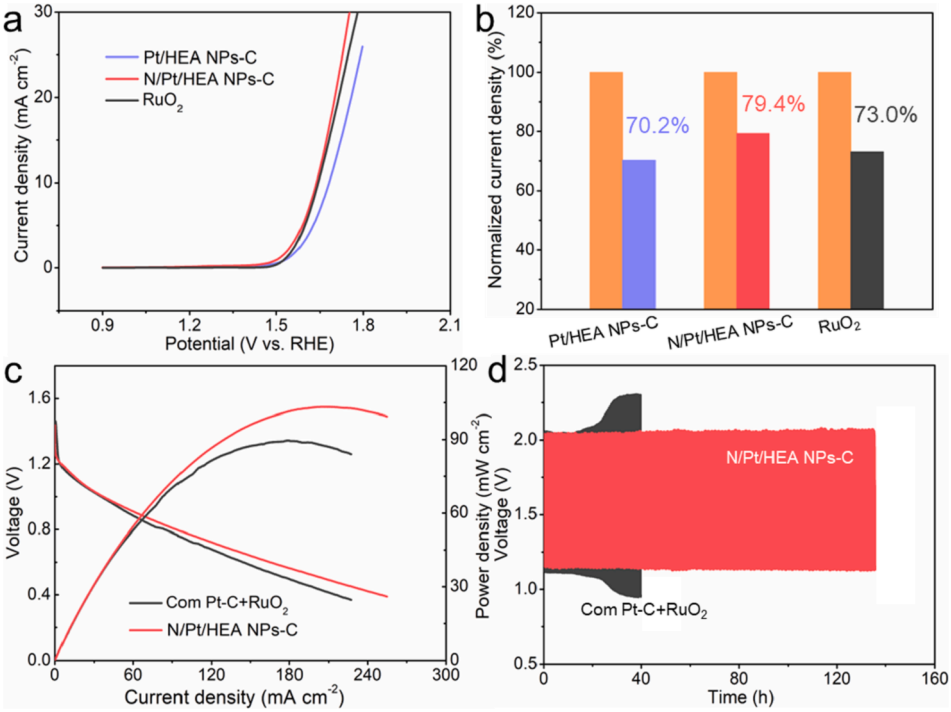

Fig. 3. (a) OER polarization curves of N/Pt/HEA NPs-C, Pt/HEA NPs-C, and RuO_2 in O_2-saturated 1.0 M KOH electrode. (b) Chronoamperometric testing of N/Pt/HEA NPs-C and RuO_2. (c) Power densities and (d) cycling stability of assembled Zn-air batteries. Current density: 10 mA cm^{-2}.

was also evaluated and compared. The mass activity evolutions of the three catalysts exhibit similar trends to that of above half-wave potentials. After 15,000 cycles, the histogram in Fig. 2f reveals that 94.6 % of its original mass activity can be maintained for N/Pt/HEA NPs-C, 84.4 % for Pt/HEA NPs-C, and 66.7 % for Com Pt-C. These findings suggest that N doping can significantly increase the durability of the high-entropy PtFeNiCoMn electrocatalyst. The TEM images of the samples after ADTs were recorded to gain the insights of morphology and composition changes. Pt/HEA NPs and N/Pt/HEA NPs still have a great dispersion on carbon support (Figure S9a-c); however, the atomic ratio of Pt/Fe/Ni/Co/Mn in Pt/HEA NPs-C results remarkable change (Table S1). This finding suggests that the transition metals in Pt/HEA NPs-C suffer bad electrochemical oxidation and leaching. While for N/Pt/HEA NPs, the elemental ratio, composition, and crystal structure are mainly maintained (Figure S9d, Figure S10a). The N–Metal bonding could also be detected even after the stability testing (Figure S10b). By contrast, Pt crystals in Com Pt-C catalyst appear severe aggregation (Figure S11). Therefore, it is believed that the high entropy effect could significantly increase the chemical stability of HEA by suppressing nanocrystal mobility and aggregation, while the dopant N plays a major role in alleviating the electrochemical leaching of transition metals for conspicuous corrosion resistance.

To further verify the beneficial effect of dopant N in HEA-based materials on maintaining the catalytic activity during the stability testing, carbon supported N doped senary PtFeNiCoMnCu NPs (N/6-Pt/HEA NPs-C) (Figures S12, 13) and carbon supported PtFeNiCoMnCu NPs without N doping (6-Pt/HEA NPs-C) were prepared, and their ORR polarization curves were measured and provided in Fig. 2g. Obviously, N/6-Pt/HEA NPs-C shows a more positive half-wave potential than 6-Pt/HEA NPs-C and Com Pt-C catalysts. Significantly, only 5 and 12 mV decays in half-wave potential were found for N/6-Pt/HEA NPs-C after 15,000 and 30,000 cycles (Fig. 2h). By contrast, 15 mV was found for 6-Pt/HEA NPs-C after 15,000 cycles (Figure S14). The histogram in Fig. 2i presents that the ORR activity of N/6-Pt/HEA NPs-C after ADT could be well maintained against those of 6-Pt/HEA NPs-C and Com Pt-C catalysts. Overall, these results confirm that the dopant N in Pt-based HEAs exhibits beneficial effect on maintaining their high ORR activity.

3.3. Electrocatalytic properties for OER and Zn-air battery

N/Pt/HEA NPs-C also presents greatly enhanced OER activity and the activity could be well maintained after stability testing in 1.0 M KOH electrolyte. As shown in Fig. 3a, the overpotential of Pt/HEA NPs-C is 411 mV at the current density of 10 mA cm^{-2}. While for N/Pt/HEA NPs-C, the overpotential is reduced to 376 mV. This value is 7 mV more negative than that of the control sample of RuO_2 (383 mV). In comparison with Pt/HEA NPs-C, N/Pt/HEA NPs-C also shows a similar advantage in overpotential when the current density was normalized with Pt loading (Figure S15). Furthermore, 71.8 % of the normalized current densities is retained for N/Pt/HEA NPs-C after chronoamperometric testing, which is much higher than that of Pt/HEA NPs-C (64.5 %) and RuO_2 (67.3 %), indicating its greater OER stability (Fig. 3b). Considering the great ORR and OER performance of N/Pt/HEA NPs-C, a rechargeable Zn-air battery was assembled to study its catalytic properties in practical operation (Fig. 3c). The Zn-air battery assembled with N/Pt/HEA NPs-C catalyst delivers a maximum power density of 160.2 mW cm^{-2}, which is greater than that of the catalyst Com Pt-C + RuO_2 (156.5 mW cm^{-2}). Additionally, in comparison with the control ZAB (20 h), the former one can stably operate at a constant working current density of 10 mA cm^{-2} for at least 135 h (Fig. 3d), demonstrating its remarkable longer charge/discharge cycling stability. Considering that the Joule heating method has the advantages of low energy consumption and fast heating rate, and the prepared N/Pt/HEA NPs-C is easy for large-scale production, the catalyst has great potential for practical application in Zn-air battery and fuel cells.

3.4. Theoretical studies of the catalytic mechanism of N/Pt/HEA NPs

Computational simulations were carried out to obtain further insights into the enhanced catalytic properties of N/Pt/HEA NPs. Fig. 4a shows the optimized crystal structures of Pt/HEA and N/Pt/HEA models (4 × 4 supercell), which suggests that the both models have 16 surface

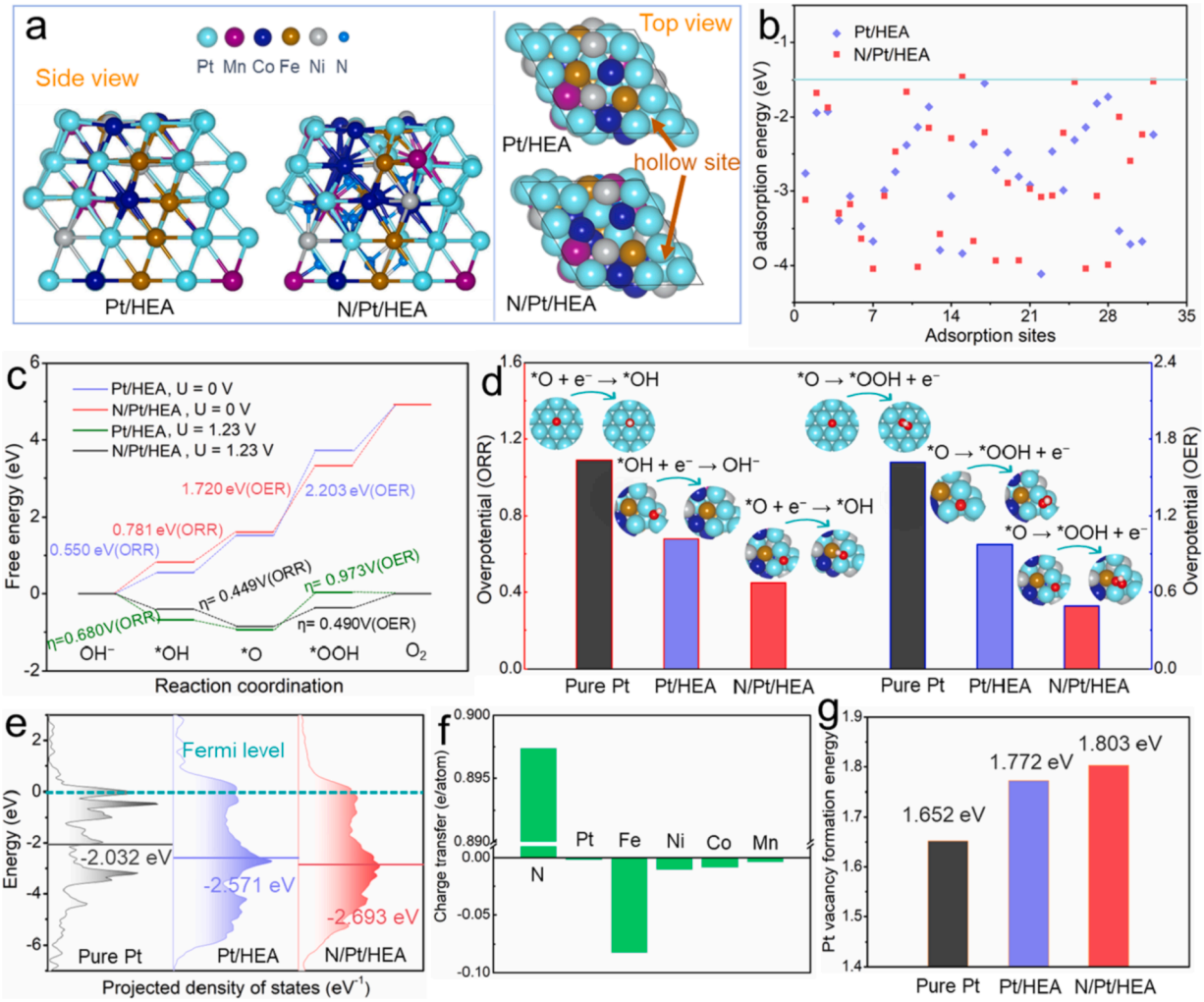

Fig. 4. (a) Side and top views of the Pt/HEA and N/Pt/HEA after structural optimization. (b) ΔE_{O^*} values of Pt/HEA and N/Pt/HEA at various hollow sites. (c) Gibbs free energy diagrams of Pt/HEA and N/Pt/HEA toward ORR and OER at 0 and 1.23 V. (d) The RDS of ORR and PDS of OER for pure Pt slab, Pt/HEA, and N/Pt/HEA. (e) The calculated projected density of states of Pt-5d-dz^2 electrons of pure Pt slab, Pt/HEA, and N/Pt/HEA. The gray, blue, and red lines stand for the d-band centers of pure Pt slab, Pt/HEA, and N/Pt/HEA, respectively. (f) The average charge transfer between surface metal atoms and dopant N in N/Pt/HEA. Negative and positive values represent the charge loss and charge accumulation, respectively. (g) The comparison of vacancy formation energy (E_{vac}) of Pt atom in pure Pt slab, Pt/HEA and N/Pt/HEA. (For interpretation of the references to colour in this figure legend, the reader is referred to the web version of this article.)

metal atoms and consequently 32 hollow sites for O atom adsorption. It is generally accepted that the atomic O adsorption energy (ΔE_{O^*}) for Pt-based structures could be served as an indicator to evaluate ORR and OER activities, and the activities are mainly limited by a strong ΔE_{O^*} [53,54]. That is, a weaker ΔE_{O^*} implies a higher catalytic activity. Fig. 4b shows the calculated ΔE_{O^*} of Pt/HEA and N/Pt/HEA at various hollow sites. The weakest ΔE_{O^*s} for Pt/HEA and N/Pt/HEA were observed at Pt-Pt-Pt hollow sites, with the values of −1.544 eV and −1.456 eV, respectively. These results indicate that N/Pt/HEA has higher intrinsic catalytic activity toward both ORR and OER than Pt/HEA, and Pt-Pt-Pt hollow sites on Pt/HEA and N/Pt/HEA could function as catalytic active sites due to the optimal positions for O atom adsorption.

The Gibbs free energies of *OH, *O and *OOH adsorption on Pt-Pt-Pt hollow sites were calculated to investigate the ORR and OER steps (Fig. 4c). For Pt/HEA, the conversion of *OH to OH^- becomes the rate determining step (RDS) toward ORR, with an overpotential (η) of 0.680 V, according to the released energy from the RDS (0.550 eV). While the potential determining step (PDS) for OER is the step of *O to *OOH, with a η of 0.973 V. By contrast, both N/Pt/HEA and Pt/HEA have the same PDS for OER, whereas the RDS of N/Pt/HEA for the ORR becomes the reaction step of *O to *OH. Significantly, the ηs of N/Pt/HEA for ORR (η^{ORR}) and OER (η^{OER}) reduce to 0.449 and 0.490 V, respectively. This result confirms higher ORR and OER activities of N/Pt/HEA compared to Pt/HEA theoretically. The RDS of ORR and PDS of OER for pure Pt slab were also calculated (Fig. 4d, Figure S16). Compared to Pt/HEA and N/Pt/HEA, pure Pt slab shows higher ηs for both ORR and OER, which should be attributed to its stronger ΔE_{O^*} [55]. Correspondingly, for Pt/HEA and N/Pt/HEA, the reduced η^{ORR} and η^{OER} should be critically attributed to the weakened adsorption of *O and *OH species due to the upshift Gibbs free energies.

The projected density of states (PDOSs) of pure Pt slab, Pt/HEA, and N/Pt/HEA were calculated to investigate the origin of the weakened adsorption energies of *O and *OH. Considering that the valence electrons in dz^2 orbital of Pt are mainly contributed to Pt − O bonding [56], the PDOSs of Pt-5d-dz^2 electrons were calculated and shown as in Fig. 4e. The d-band center of N/Pt/HEA (−2.693 eV) downshifts to a more negative position in comparison with that of Pt/HEA (−2.571 eV), indicating that the dopant N enables the d-band center of Pt-5d-dz^2 electrons away from the Fermi level, consequently resulting in a weakened ΔE_{O^*} for greater ORR and OER activities. Moreover, in comparison with pure Pt slab (2.056 Å) and Pt/HEA (2.075 Å), the average length of Pt–O bond on N/Pt/HEA is stretched to 2.080 Å, confirming its weakened ΔE_{O^*}. Previous literatures had demonstrated that compressive

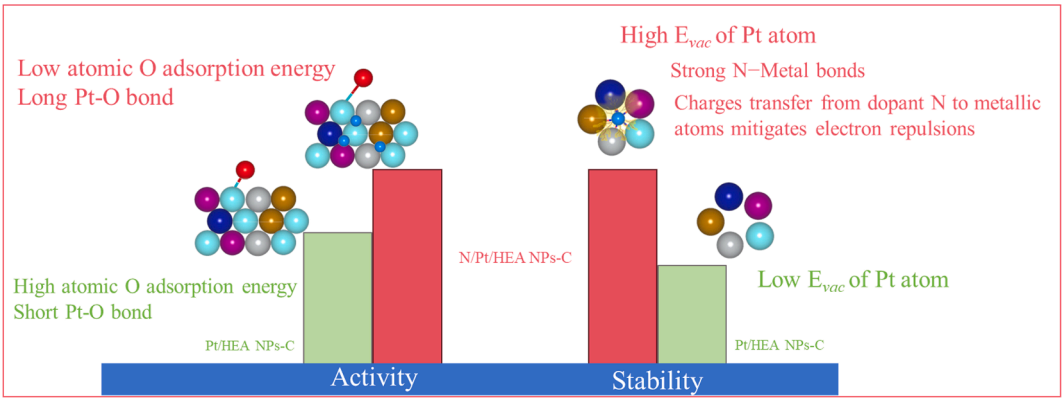

Fig. 5. Scheme of the catalysis enhancement mechanism of N/Pt/HEA NPs-C.

surface strain usually play a critical role in boosting activity in oxygen electrocatalysis [53,57]. It is believed that the compressive strains in both Pt/HEA and N/Pt/HEA also contribute to the weakened ΔE_{O^*} for high activity.

To reveal the origin of the enhanced electrochemical stability of N/Pt/HEA NPs, the average charge transfer between dopant N and surface metal atoms, and vacancy formation energy (E_{vac}) of Pt in Pt/HEA, N/Pt/HEA, and pure Pt slab systems were calculated. The Bader charge analysis results shown in Fig. 4f reveal a distinct charge transfer from dopant N to surface atoms in N/Pt/HEA, consistent with the XPS results in Fig. 1f. It is noted that the charge transfer might also exist between carbon materials and alloys, influencing the catalytic properties of N/Pt/HEA NPs-C [58–60]. Generally, a higher E_{vac} of the surface metal atom on a crystal suggests a better structural stability [61]. Obviously, in comparison with the pure Pt slab (1.652 eV) and Pt/HEA (1.772 eV), the N/Pt/HEA (1.803 eV) has a higher E_{vac} of Pt atom (Fig. 4g and S17). These findings demonstrate a higher structural stability of N/Pt/HEA NPs compared to Pt/HEA NPs. The N – Metal bonds and dopant N contribute to the high E_{vac} of Pt in N/Pt/HEA NPs, accounting for the observed outstanding structural stability. Especially, the dopant N plays a critical role in fine-tuning the electronic structure of the metals in N/Pt/HEA NPs, which mitigates the electron repulsions among the metallic atoms because of a higher electronegativity of N relative to the metals in N/Pt/HEA NPs. The strong N – Metal bonds are responsible for retarding the oxidative dissolution and electrochemical leaching of metals. The improvement of the electrocatalytic properties due to N doping is schematically illustrated in Fig. 5.

4. Conclusions

In summary, N doping in Pt-based high-entropy nanoalloys is achieved via a rapid Joule heating method. A N-doped PtFeNiCoMn nanoalloy catalyst supported on XC-72 carbon shows significantly improved stability and enhanced catalytic activities in comparison with its counterpart (i.e., PtFeNiCoMn without N doping) and Commercial Pt/C catalysts in both oxygen reduction and oxygen evolution reactions. 94.6 % activity of the N-doped PtFeNiCoMn nanoalloy in the oxygen reduction reaction is maintained after continuous 15,000 cycles, in sharp contrast to 84.4 % activity maintenance of the PtFeNiCoMn nanoalloy without N doping. The improved stability is also observed from the oxygen evolution reaction and a Zn-air battery full cell. Computational calculation results reveal that the dopant N optimizes the electronic state of Pt by downshifting its d-band center, resulting in a weakened adsorption energy of O and consequently great activity in oxygen electrocatalysis. While the origin of the high stability of N-doped PtFeNiCoMn nanoalloy should be attributed to dopant N coupled with the formation of N – metal bonds, leading to an increase in the vacancy formation energy of Pt. Especially, the N-doping mitigates the electron repulsions among the metallic atoms because of a higher electronegativity of N compared to the transition metals. The strong N – Metal bonds are responsible for retarding the oxidative dissolution and electrochemical leaching of metals. Our future studies will focus on optimizing the molar ratio of introduced transitional metals, followed by investigating the changes in ORR activity and stability. This work offers a low Pt loading, active and stable multifunctional electrocatalyst, and demonstrates an effective strategy to improving the stability of catalysts by increasing the vacancy formation energy for energy conversion and beyond.

CRediT authorship contribution statement

Mang Niu: Writing – original draft, Software, Methodology, Investigation. **Qinhe Guan:** Writing – original draft, Investigation, Data curation. **Weiyong Yuan:** Writing – review & editing, Methodology. **Chun Xian Guo:** Supervision, Formal analysis. **Dapeng Cao:** Software. **Chang Ming Li:** Writing – review & editing, Supervision. **Lian Ying Zhang:** Writing – review & editing, Supervision, Conceptualization. **Xiu Song Zhao:** Writing – review & editing, Supervision.

Declaration of competing interest

The authors declare that they have no known competing financial interests or personal relationships that could have appeared to influence the work reported in this paper.

Acknowledgments

We gratefully acknowledge to the financial support from the National Natural Science Foundation of China (22379078).

Appendix A. Supplementary data

Supplementary data to this article can be found online at https://doi.org/10.1016/j.cej.2024.158465.

Data availability

Data will be made available on request.

References

[1] Y. Yao, Z. Huang, P. Xie, S.D. Lacey, R.J. Jacob, H. Xie, F. Chen, A. Nie, T. Pu, M. Rehwoldt, Carbothermal shock synthesis of high-entropy-alloy nanoparticles, Science 359 (2018) 1489–1494.
[2] W. Zhu, X. Gao, Y. Yao, S. Hu, Z. Li, Y. Teng, H. Wang, H. Gong, Z. Chen, Y. Yang, Nanostructured high entropy alloys as structural and functional materials, ACS Nano 18 (2024) 12672–12706.

[3] J.T. Ren, L. Chen, H.Y. Wang, Z.Y. Yuan, High-entropy alloys in electrocatalysis: from fundamentals to applications, Chem. Soc. Rev. 52 (2023) 8319–8373.
[4] T.Y. Lin, F.Y. Yen, Y.C. Ting, P.W. Chen, S.Y. Lu, Non-precious bifunctional high entropy alloy catalyst and layered double hydroxide enhanced gel electrolyte based rechargeable flexible zinc-air batteries, Chem. Eng. J. 488 (2024) 151093.
[5] L. Tao, M. Sun, Y. Zhou, M. Luo, F. Lv, M. Li, Q. Zhang, L. Gu, B. Huang, S. Guo, A general synthetic method for high-entropy alloy subnanometer ribbons, J. Am. Chem. Soc. 144 (2022) 10582–10590.
[6] J. Shen, Z. Hu, K. Chen, C. Chen, Y. Zhu, C. Li, Platinum based high entropy alloy oxygen reduction electrocatalysts for proton exchange membrane fuel cells, Mater. Today Nano 21 (2023) 100282.
[7] T.H. Yang, J. Ahn, S. Shi, P. Wang, R. Gao, D. Qin, Noble-metal nanoframes and their catalytic applications, Chem. Rev. 121 (2021) 796–833.
[8] L.Y. Zhang, T. Zeng, L. Zheng, Y. Wang, W. Yuan, M. Niu, C.X. Guo, D. Cao, C.M. Li, Epitaxial growth of Pt–Pd bimetallic heterostructures for the oxygen reduction reaction, Adv. Powder Mater. 2 (2023) 100131.
[9] Y. Shi, Z. Lyu, M. Zhao, R. Chen, Q.N. Nguyen, Y. Xia, Noble-Metal nanocrystals with controlled shapes for catalytic and electrocatalytic applications, Chem. Rev. 121 (2021) 649–735.
[10] G. Feng, F. Ning, Y. Pan, T. Chen, J. Song, Y. Wang, R. Zou, D. Su, D. Xia, Engineering structurally ordered high-entropy intermetallic nanoparticles with high-activity facets for oxygen reduction in practical fuel cells, J. Am. Chem. Soc. 145 (2023) 11140–11150.
[11] A.V. Rozhkov, D.M. Ivanov, A.S. Novikov, I.V. Ananyev, N.A. Bokach, V. Y. Kukushkin, Metal-involving halogen bond Ar-I center dot center dot center dot in a platinum acetylacetonate complex, CrstEngComm 22 (2020) 554–563.
[12] H. Li, M. Sun, Y. Pan, J. Xiong, H. Du, Y. Yu, S. Feng, Z. Li, J. Lai, B. Huang, L. Wang, The self-complementary effect through strong orbital coupling in ultrathin high-entropy alloy nanowires boosting pH-universal multifunctional electrocatalysis, Appl. Catal. B-Environ. 312 (2022) 121431.
[13] W. Zhang, X. Feng, Z.X. Mao, J. Li, Z. Wei, Stably immobilizing sub-3 nm high-entropy Pt alloy nanocrystals in porous carbon as durable oxygen reduction electrocatalyst, Adv. Funct. Mater. 32 (2022) 2204110.
[14] C. Zhan, L. Bu, H. Sun, X. Huang, Z. Zhu, T. Yang, H. Ma, L. Li, Y. Wang, H. Geng, W. Wang, H. Zhu, C.W. Pao, Q. Shao, Z. Yang, W. Liu, Z. Xie, X. Huang, Medium/high-entropy amalgamated core/shell nanoplate achieves efficient formic acid catalysis for direct formic acid fuel cell, Angew. Chem. Int. Ed. 62 (2023) e202213783.
[15] H. Bian, P. Qi, G. Xie, X. Liu, Y. Zeng, D. Zhang, P. Wang, HEA-NiFeCuCoCe/NF through ultra-fast electrochemical self-reconstruction with high catalytic activity and corrosion resistance for seawater electrolysis, Chem. Eng. J. 477 (2023) 147286.
[16] V.H. Do, J.M. Lee, Surface engineering for stable electrocatalysis, Chem. Soc. Rev. 53 (2024) 2693–2737.
[17] T. Loffler, A. Ludwig, J. Rossmeisl, W. Schuhmann, What makes high-entropy alloys exceptional electrocatalysts? Angew. Chem. Int. Ed. 60 (2021) 26894–26903.
[18] W. Shi, H. Liu, Z. Li, C. Li, J. Zhou, Y. Yuan, F. Jiang, K. Fu, Y. Yao, Highentropy alloy stabilized and activated Pt clusters for highly efficient electrocatalysis, SusMat 2 (2022) 186–196.
[19] W. Chen, S. Luo, M. Sun, X. Wu, Y. Zhou, Y. Liao, M. Tang, X. Fan, B. Huang, Z. Quan, High-entropy intermetallic PtRhBiSnSb nanoplates for highly efficient alcohol oxidation electrocatalysis, Adv. Mater. 34 (2022) 2206276.
[20] B.A. Lu, L.F. Shen, J. Liu, Q. Zhang, L.Y. Wan, D.J. Morris, R.X. Wang, Z.Y. Zhou, G. Li, T. Sheng, Structurally disordered phosphorus-doped Pt as a highly active electrocatalyst for an oxygen reduction reaction, ACS Catal. 11 (2020) 355–363.
[21] X. Zhao, C. Xi, R. Zhang, L. Song, C. Wang, J.S. Spendelow, A.I. Frenkel, J. Yang, H. L. Xin, K. Sasaki, High-performance nitrogen-doped intermetallic PtNi catalyst for the oxygen reduction reaction, ACS Catal. 10 (2020) 10637–10645.
[22] Y. Xiong, Y. Ma, L. Zou, S. Han, H. Chen, S. Wang, M. Gu, Y. Shen, L. Zhang, Z. Xia, N-doping induced tensile-strained Pt nanoparticles ensuring an excellent durability of the oxygen reduction reaction, J. Catal. 382 (2020) 247–255.
[23] Z. Mao, C. Ding, X. Liu, Q. Zhang, X. Qin, H. Li, F. Yang, Q. Li, X.G. Zhang, J. Zhang, Interstitial B-doping in Pt lattice to upgrade oxygen electroreduction performance, ACS Catal. 12 (2022) 8848–8856.
[24] M. Klimova, D. Shaysultanov, A. Semenyuk, S. Zherebtsov, G. Salishchev, N. Stepanov, Effect of nitrogen on mechanical properties of CoCrFeMnNi high entropy alloy at room and cryogenic temperatures, J. Alloy. Compd. 849 (2020) 156633.
[25] X. Zhao, H. Cheng, X. Chen, Q. Zhang, C. Li, J. Xie, N. Marinkovic, L. Ma, J. C. Zheng, K. Sasaki, Multiple metal–nitrogen bonds synergistically boosting the activity and durability of high-entropy alloy electrocatalysts, J. Am. Chem. Soc. 146 (2024) 3010–3022.
[26] T. Chen, C. Foo, S.C.E. Tsang, Interstitial and substitutional light elements in transition metals for heterogeneous catalysis, Chem. Sci. 12 (2021) 517–532.
[27] Y.C. Qin, F.Q. Wang, X.M. Wang, M.W. Wang, W.L. Zhang, W.K. An, X.P. Wang, Y. L. Ren, X. Zheng, D.C. Lv, A. Ahmad, Noble metal-based high-entropy alloys as advanced electrocatalysts for energy conversion, Rare Met. 40 (2021) 2354–2368.
[28] B. Peng, Z. Liu, L. Sementa, Q. Jia, Q. Sun, C.U. Segre, E. Liu, M. Xu, Y.-H. Tsai, X. Yan, Z. Zhao, J. Huang, X. Pan, X. Duan, A. Fortunelli, Y. Huang, Embedded oxide clusters stabilize sub-2 nm Pt nanoparticles for highly durable fuel cells, Nat. Catal. (2024) 1–11.
[29] Y. Zhang, B. Chen, Y. Qiao, Y. Duan, X. Qi, S. He, H. Zhou, J. Chen, A. Yuan, S. Zheng, FeNi alloys incorporated N-doped carbon nanotubes as efficient bifunctional electrocatalyst with phase-dependent activity for oxygen and hydrogen evolution reactions, J. Mater. Sci. Technol. 201 (2024) 157–165.
[30] X. Wang, M. Yu, X. Feng, Electronic structure regulation of noble metal-free materials toward alkaline oxygen electrocatalysis, eScience, 3 (2023) 100141.
[31] K. Gong, F. Du, Z. Xia, M.F. Durstock, L. Dai, Nitrogen-doped carbon nanotube arrays with high electrocatalytic activity for oxygen reduction, Science 323 (2009) 760–764.
[32] S. He, B. Chen, C. Meng, F. Shi, A. Yuan, W. Miao, H. Zhou, Coupling $NiSe_2$ nanoparticles with N-doped porous carbon enables efficient and durable electrocatalytic hydrogen evolution reaction at pH values ranging from 0 to 14, ACS Appl. Nano Mater. 7 (2023) 1138–1145.
[33] Y. Shen, S. He, Y. Zhuang, S. Huang, C. Meng, A. Yuan, W. Miao, H. Zhou, Polypyrrole template-assisted synthesis of tubular Fe-NC nanostructure-based electrocatalysts for efficient oxygen reduction reaction in rechargeable Zinc–air battery, ACS Appl. Nano Mater. 6 (2023) 16873–16881.
[34] D. Lu, X. Fu, D. Guo, W. Ma, S. Sun, G. Shao, Z. Zhou, Challenges and opportunities in 2D high-entropy alloy electrocatalysts for sustainable energy conversion, SusMat 3 (2023) 730–748.
[35] J. Scharf, M. Kübler, V. Gridin, W.D.Z. Wallace, L. Ni, S.D. Paul, U.I. Kramm, Relation between half-cell and fuel cell activity and stability of FeNC catalysts for the oxygen reduction reaction, SusMat 2 (2022) 630–645.
[36] M. Escuderoescribano, P. Malacrida, M.H. Hansen, U.G. Vejhansen, A. Velazquezpalenzuela, V. Tripkovic, J. Schiotz, J. Rossmeisl, I.E.L. Stephens, I. Chorkendorff, Tuning the activity of Pt alloy electrocatalysts by means of the lanthanide contraction, Science 352 (2016) 73–76.
[37] H. Yu, T. Zhou, Z. Wang, Y. Xu, X. Li, L. Wang, H. Wang, Defect-rich porous palladium metallene for enhanced alkaline oxygen reduction electrocatalysis, Angew. Chem. Int. Ed. 133 (2021) 12134–12138.
[38] X. Ge, W.Y. Yuan, Q. Guan, L.Y. Zhang, A universal strategy for green and surfactant-free synthesis of noble metal nanoparticles, Chem. Commun. 60 (2024) 722–725.
[39] L.Y. Zhang, C.X. Guo, H. Cao, S. Wang, Y. Ouyang, B. Xu, P. Guo, C.M. Li, Highly wrinkled palladium nanosheets as advanced electrocatalysts for the oxygen reduction reaction in acidic medium, Chem. Eng. J. 431 (2022) 133237.
[40] R. Guo, K. Zhang, Y. Liu, Y. He, C. Wu, M. Jin, Hydrothermal synthesis of palladium nitrides as robust multifunctional electrocatalysts for fuel cells, J. Mater. Chem. A 9 (2021) 6196–6204.
[41] S. Wang, B. Xu, W. Huo, H. Feng, X. Zhou, F. Fang, Z. Xie, J.K. Shang, J. Jiang, Efficient FeCoNiCuPd thin-film electrocatalyst for alkaline oxygen and hydrogen evolution reactions, Appl. Catal. B-Environ. 313 (2022) 121472.
[42] X. Tian, X. Zhao, Y.Q. Su, L. Wang, H. Wang, D. Dang, B. Chi, H. Liu, E.J. Hensen, X.W.D. Lou, Engineering bunched Pt-Ni alloy nanocages for efficient oxygen reduction in practical fuel cells, Science 366 (2019) 850–856.
[43] T. Zeng, M. Niu, B. Xu, W. Yuan, C.X. Guo, D. Cao, C.M. Li, L.Y. Zhang, X.S. Zhao, Control over nitrogen dopant sites in palladium metallene for manipulating catalytic activity and stability in the oxygen reduction reaction, Adv. Funct. Mater. (2024) 2408264.
[44] G. Soto, W.D.L. Cruz, M.H. Farias, XPS, AES, and EELS characterization of nitrogen-containing thin films, J. Electron. Spectrosc. Relat. Phenom. 135 (2004) 27–39.
[45] C. Hess, New advances in using Raman spectroscopy for the characterization of catalysts and catalytic reactions, Chem. Soc. Rev. 50 (2021) 3519–3564.
[46] B. Jia, B. Zhang, Z. Cai, X. Yang, L. Li, L. Guo, Construction of amorphous/crystalline heterointerfaces for enhanced electrochemical processes, eScience 3 (2023) 100112.
[47] D. Wu, C. Wang, H. Wu, S. Wang, F. Wang, Z. Chen, T. Zhao, Z. Zhang, L.Y. Zhang, C.M. Li, Synthesis of hollow Co_3O_4 nanocrystals in situ anchored on holey graphene for high-rate lithium-ion batteries, Carbon 163 (2020) 137–144.
[48] D. Wang, H.L. Xin, R. Hovden, H. Wang, Y. Yu, D.A. Muller, F.J. Disalvo, H. D. Abruna, Structurally ordered intermetallic platinum–cobalt core–shell nanoparticles with enhanced activity and stability as oxygen reduction electrocatalysts, Nat. Mater. 12 (2012) 81–87.
[49] T. Zeng, X. Meng, H. Huang, L. Zheng, H. Chen, Y. Zhang, W. Yuan, L.Y. Zhang, Controllable synthesis of web-footed PdCu nanosheets and their electrocatalytic applications, Small 18 (2022) 2107623.
[50] T. Chen, D. Liu, X.L. Li, M.Q. Shi, Z.H. Xiang, A mass transfer-enhanced pyrolysis-free bifunctional catalyst to boost ultralong lifespan zinc-air batteries, Energy Mater. Adv. 4 (2023) 0061.
[51] L. Zheng, M. Niu, T. Zeng, X. Ge, Y. Wang, C.X. Guo, W. Yuan, D. Cao, L.Y. Zhang, C.M. Li, Assembling molybdenum-doped platinum clusters into a coral-like nanostructure for highly enhanced oxygen reduction, eScience 4 (2024) 100187.
[52] S. Chen, J. Zhao, H. Su, H. Li, J. Zeng, Pd–Pt tesseracts for the oxygen reduction reaction, J. Am. Chem. Soc. 143 (2021) 496–503.
[53] L. Wang, Z. Zeng, W. Gao, T. Maxson, D. Raciti, M. Giroux, X. Pan, C. Wang, J. Greeley, Tunable intrinsic strain in two-dimensional transition metal electrocatalysts, Science 363 (2019) 870–874.
[54] P. Strasser, S. Koh, T. Anniyev, J. Greeley, K. More, C. Yu, Z. Liu, S. Kaya, D. Nordlund, H. Ogasawara, Lattice-strain control of the activity in dealloyed core–shell fuel cell catalysts, Nat. Chem. 2 (2010) 454.
[55] J. Greeley, I. Stephens, A. Bondarenko, T.P. Johansson, H.A. Hansen, T. Jaramillo, J. Rossmeisl, I. Chorkendorff, J.K. Nørskov, Alloys of platinum and early transition metals as oxygen reduction electrocatalysts, Nat. Chem. 1 (2009) 552–556.
[56] Y. Chen, F. Sun, Q. Tang, Computational insights and design of promising ultrathin pdm bimetallenes for oxygen reduction electrocatalysis, Small Methods 7 (2023) 2300276.
[57] L. Bu, N. Zhang, S. Guo, X. Zhang, J. Li, J. Yao, T. Wu, G. Lu, J. Ma, D. Su, Biaxially strained PtPb/Pt core/shell nanoplate boosts oxygen reduction catalysis, Science 354 (2016) 1410–1414.

[58] W. Si, Q. Liao, Y. Li, H. Zhao, A.S. Novikov, L. Qin, Growth behavior of anisotropic monometallic MOFs derivatives with the high absorbing and thermal properties, J. Alloy. Compd. 1007 (2024) 176398.
[59] R. Paul, Q. Zhai, A.K. Roy, L. Dai, Charge transfer of carbon nanomaterials for efficient metal-free electrocatalysis, Interdiscip Mater. 1 (2022) 28–50.
[60] Y.A. Mezenov, S. Bruyere, A. Krasilin, E. Khrapova, S.V. Bachinin, P. V. Alekseevskiy, S. Shipiloskikh, P. Boulet, S. Hupont, A. Nomine, Insights into solid-to-solid transformation of MOF amorphous phases, Inorg. Chem. 61 (2022) 13992–14003.
[61] H. Huang, K. Li, Z. Chen, L. Luo, Y. Gu, D. Zhang, C. Ma, R. Si, J. Yang, Z. Peng, Achieving remarkable activity and durability toward oxygen reduction reaction based on ultrathin Rh-doped Pt nanowires, J. Am. Chem. Soc. 139 (2017) 8152–8159.